Journal of Materials Chemistry A

ROYAL SOCIETY OF CHEMISTRY

PAPER

View Article Online
View Journal | View Issue

Cite this: J. Mater. Chem. A, 2024, 12, 28056

Interfacial integration of ultra-thin flexible electrochemical capacitors *via* vacuum filtration based on gelatinized fibrous membranes†

Qian Xie,‡[a] Chengjie Lu,‡[a] Chengjie Yi,[a] Tao Shui,*[a] Nosipho Moloto,[b] Jiacheng Liu,[c] Song-Zhu Kure-Chu,[c] Takehiko Hihara,[c] Wei Zhang *[a] and ZhengMing Sun *[a]

Received 23rd July 2024
Accepted 22nd September 2024

DOI: 10.1039/d4ta05110f

rsc.li/materials-a

Hydrogel electrolytes have been widely used for constructing flexible electrochemical capacitors. However, the weak interface bonding between hydrogel electrolytes and electrode materials often leads to a deterioration of the electrochemical performance during deformation. Herein, a universal fabrication method utilizing vacuum filtration was developed to ensure a robust electrode–electrolyte interface. By *in situ* gelation of fibrous membranes, we overcome the hurdle of hydrogel filtration, enabling the construction of ultra-thin all-in-one electrochemical capacitors. This strategy has been demonstrated as a universal platform for constructing paper-like devices with an all-in-one structure that is applicable to a variety of electrochemical energy storage systems, including symmetric supercapacitors, asymmetric supercapacitors, ammonium-ion hybrid capacitors, and zinc-ion hybrid capacitors. Among these, the zinc-ion hybrid capacitors demonstrate a high specific capacitance of 474.1 F g^{-1} and a high energy density of 41.8 mW h cm^{-3}. Additionally, series-connected electrochemical capacitors can power devices under deformations of bending, folding, and curling, showcasing the potential application of wearable energy storage.

1. Introduction

In light of the significant advancements in wearable electronics,[1–3] flexible electrochemical capacitors have been considered as important energy storage devices due to their high power density and long cycling stability.[4,5] Owing to their exceptional flexibility, high ion conductivity, and leak prevention properties, hydrogels have found extensive application for flexible electrolytes.[6,7] Based on the outstanding intrinsic properties of hydrogels, a large number of multifunctional flexible hydrogel capacitors with excellent performance have emerged in recent years.[8–11] However, wet and soft hydrogel electrolytes are mechanically incompatible with electrodes and exhibit poor interface adhesion, consequently compromising the integrity of flexible devices.[12] As a result, the conventional sandwich structure, primarily based on the mechanical assembly of flexible electrodes and hydrogel electrolytes, often leads to interfacial failure and large interfacial resistance, which will subsequently deteriorate the electrochemical performance of the device.[13] For a stable and robust interface plays such a crucial role for the electrochemical performance and cycling life of the flexible electrochemical capacitors, it is essential to address the challenges of interface integration between the hydrogel electrolyte and the electrodes.

To address the problem of weak interfacial contact between electrodes and hydrogel electrolytes, one strategy is to construct robust interfacial adhesion through hydrogen bonding between the hydrogel electrode and hydrogel electrolyte, achieving the integration of all components in electrochemical capacitors.[14,15] Although this approach effectively achieves low charge transfer resistance, the hydrogel electrode is predominantly composed of non-electrochemically active polymers and water, resulting in low active materials loading, and a decline in specific capacitance and energy density. To maintain optimal electrode performance, *in situ* polymerization of the electrode layer on the hydrogel surface may construct an integrated structure comprising conductive polymer electrodes and hydrogel electrolytes.[16,17] However, controlling the mass loading of the electrode materials can be challenging as it is difficult to precisely control the degree of polymerization. In addition, the range of electrode materials amenable to polymerization is limited, typically based on a few conductive polymers such as

[a]School of Materials Science and Engineering, Southeast University, Nanjing, 211189, China. E-mail: w69zhang@seu.edu.cn; tshui@seu.edu.cn; zmsun@seu.edu.cn

[b]Molecular Science Institute, School of Chemistry, University of the Witwatersrand, Private Bag 3, Wits 2050, South Africa

[c]Department of Materials Function and Design, Nagoya Institute of Technology, Gokiso-cho, Showa-ku, Nagoya, Aichi, 466-8555, Japan

† Electronic supplementary information (ESI) available. See DOI: https://doi.org/10.1039/d4ta05110f

‡ Qian Xie and Chengjie Lu contributed equally to this work.

polyaniline (PANI),[18] polypyrrole (PPy),[19] and poly(3,4-ethylenedioxythiophene) (PEDOT).[20] Therefore, it is highly desired to develop a universal strategy for achieving excellent interface contact of hydrogel-based flexible electrochemical capacitors, while ensuring superior and tunable electrode electrochemical performance.

To mitigate the problem of inadequate solid–solid interface contact, it can be a viable strategy to incorporate electrode active materials onto a porous matrix through external pressure, thereby facilitating the formation of a close interface.[21,22] For example, carbon nanotubes can be loaded on a polyamide nanofiber membrane through vacuum filtration to construct a compact all-in-one electrochemical capacitor.[23] The fibrous membrane acts as a filter paper that effectively immobilizes the active materials in the dispersion solution onto the porous fibrous network. However, since the filter paper cannot accommodate electrolytes, additional hydrogel electrolyte is still required. This inspires a strategy to use hydrogels instead of filter paper to directly immobilize electrodes on the hydrogel electrolyte through vacuum filtration, achieving an optimal solid–solid contact between the electrode and hydrogel electrolyte. However, the elastic grid-like gel network of hydrogels entraps a large amount of bound water, impeding the solvent penetration of the electrode dispersion fluid.[24,25] Consequently, the hydrogel electrolyte is difficult to directly utilize as a flexible filter paper to construct a compact and reliable interface.

Herein, we apply an *in situ* cross-linking strategy to convert the porous fiber membrane into a hydrogel after tightly bonding different electrode materials through external pressure, ultimately constructing all-in-one flexible electrochemical capacitors with rapid interfacial electrochemical kinetics between the electrolytes and electrodes. Fig. 1 outlines the general preparation procedure for an all-in-one electrochemical capacitor with a sandwich structure. By vacuum filtrating active materials on flexible PAN/PVA membranes, the electrode can be firmly secured and its thickness can be precisely controlled by adjusting the amount of active material. Additionally, a hydrogel electrolyte with 3D porous network structure is formed from the fibrous membrane by chemically cross-linking the hydroxyl groups of PVA with glutaraldehyde (GA) cross-linker, which can efficiently absorb the electrolyte solution and form a robust electrode–electrolyte interface. This approach can be applied to a wide range of electrode materials that can be dispersed in solvents, including zero-dimensional nanoparticles, one-dimensional nanowires, and two-dimensional nanosheets. This enables efficient integration of different electrode materials and serves as a versatile platform for fabricating flexible and ultra-thin energy storage devices. Various all-in-one electrochemical capacitors have been fabricated, including MXene symmetric supercapacitors, MXene//PANI asymmetric supercapacitors, PANI//NVO ammonium ion hybrid capacitors, and ZVO//NVO zinc ion hybrid capacitors, exhibiting outstanding specific capacitance and volumetric energy density. Through this strategy, these porous interface-integrated structural devices not only exhibit improved electrochemical performance but also possess exceptional flexibility imparted by their flexible structure, which has been demonstrated by finite element simulations. Furthermore, the thickness of these devices can be controlled to only 70 μm, which is thinner than A4 paper, resulting in shorter ion transport distances, larger volumetric

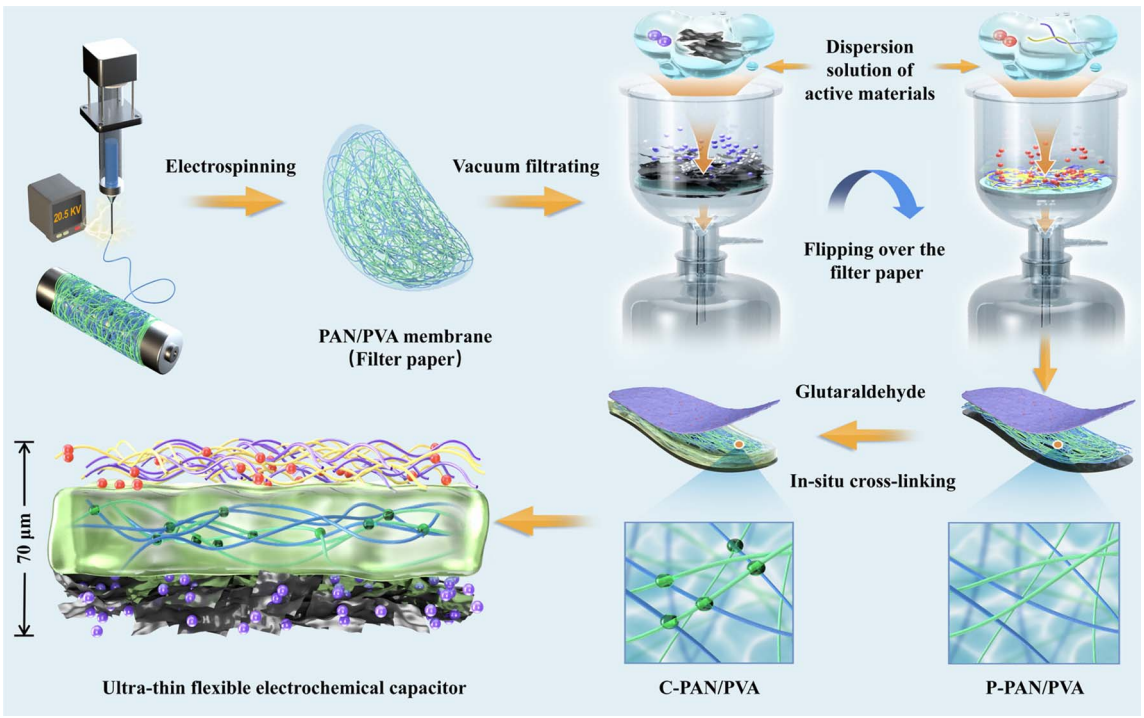

Fig. 1 Schematic diagram of preparing all-in-one electrochemical capacitors using *in situ* cross-linking strategy.

energy density, and paper-like folding flexibility, enabling its application in lightweight, conformable, and permeable wearable devices.

2. Results and discussion

The fabrication process of all-in-one electrochemical capacitors based on an *in situ* cross-linking strategy is illustrated in Fig. 1. The PAN/PVA spinning solution was first prepared by dissolving PAN and PVA in DMSO. Hydrophobic PAN exhibits excellent fiber formation properties, while the introduction of PVA brings in hydrophilic hydroxyl groups. Due to the presence of intermolecular interactions between the nitrile groups of PAN and the hydroxyl groups of PVA, they exhibited excellent miscibility in DMSO.[26] Electrospinning technology was then employed using the spinning solution to fabricate porous physically intertwined PAN/PVA membranes (P-PAN/PVA). After loading the electrode material on both sides of the P-PAN/PVA membrane through vacuum filtration, GA was employed as the cross-linker to chemically cross-link the membrane under acidic environments.[27] The hydroxyl group of PVA underwent an aldol condensation reaction with the aldehyde group of GA, resulting in the formation of ether bonds and the establishment of chemically cross-linked PAN/PVA (C-PAN/PVA) membranes. Consequently, the PVA fibers within the P-PAN/PVA membranes underwent transformation into PVA hydrogels, which not only enhanced the stability and rendered them insoluble in water, but also enabled them to absorb and accommodate aqueous electrolytes.

As shown in Fig. 2a, large-area PAN/PVA membranes can be prepared with a thickness of only 64 μm, even less than that of an A4 paper (104 μm). At the microscale level, the SEM images of PAN/PVA before and after a 1 hour cross-linking process are presented in Fig. 2b and c. The P-PAN/PVA exhibits a porous structure comprising interconnected nanofibers with an approximate diameter of 200 nm, while the cross-linked sample reveals the phenomenon of fiber fusion, which serves as cross-linking points. To verify the cross-linking process, the Fourier transform infrared (FTIR) spectra of P-PAN/PVA and C-PAN/PVA are presented in Fig. 2d. P-PAN/PVA unveils a characteristic peak at 1095 cm^{-1}, originating from the C–O groups within the PVA chain. Upon cross-linking with GA, two new peaks at 1128 cm^{-1} and 1000 cm^{-1} become evident, corresponding to the C–O–C stretching vibration of the acetal ring and the formation of ether linkages, thereby confirming successful cross-linking. To demonstrate the successful cross-linking, Fig. 2e and f present the XPS C 1s spectra of P-PAN/PVA and C-PAN/PVA. It can be observed that the peak intensity at 286.23 eV weakened after cross-linking, indicating a reduction in C–O bonds and the appearance of a peak corresponding to C═O bonds, which confirms the introduction of aldehyde groups and reflects the occurrence of cross-linking. To further validate the cross-linking of PAN/PVA with GA, the stress–strain curves of PAN/PVA before and after cross-linking are shown in Fig. 2g. The tensile strength of P-PAN/PVA reached 3.8 MPa with an elongation of 17%. After cross-linking, the tensile strength of C-PAN/PVA increased to 8.9 MPa, while the elongation decreased to 8.4%, which can be attributed to the increased number of cross-linking points in the polymer network, resulting in a more stable and stronger cross-linked network. Moreover, the C-PAN/PVA possesses enhanced water retention of 92% (7 days) (Fig. 2h). Swelling experiments showed that the PAN/PVA membrane can absorb 200% of its mass in water. However, due to the presence of PVA, the membrane exhibits a dissolution phenomenon after prolonged water immersion. Therefore, to enable its long-term use as an electrolyte, it is necessary to enhance the suppression of PVA dissolution and increase the content of insoluble gel. With a longer cross-linking time, the content of gel that swells but does not dissolve also increases from 45.7% to 89.6% (Fig. 2i). As another piece of evidence, the cross-linking density of PVA in PAN/PVA gradually increased with longer cross-linking time. For a 4 hours cross-linking duration, the cross-linking density of C-PAN/PVA was approximately 0.0119 mol cm^{-3}, significantly higher than the 0.0029 mol cm^{-3} of P-PAN/PVA (Table S1†).

For the C-PAN/PVA membrane that can accommodate the electrolyte solution, MXene symmetric supercapacitors (SSCs) were prepared by absorbing 1 M H_2SO_4 solution. Fig. 3a depicts photographs of SSCs based on MXene electrodes, which has garnered significant research interest as a high-performance two-dimensional material.[28] These all-in-one devices exhibit superior flexibility, allowing them to be wrapped around a glass rod. Fig. 3b provides a cross-sectional SEM image of the sandwich-like MXene SSC, featuring a compact integration between MXene electrodes and the porous C-PAN/PVA membrane. The device's total thickness is also measured to be approximately 70 μm. In Fig. 3c, EDS spectra demonstrate a uniform distribution and fusion of the electrode (represented by Ti signals) on both sides of the hydrogel membrane (represented by N signals), resulting in an integrated interface that facilitates rapid ion transport. Moreover, benefiting from the all-in-one structure supported by the flexible hydrogel membrane, the device can maintain its structural and performance stability under various deformations, as demonstrated by finite element simulations. Since the porous PAN/PVA membrane bonded with electrodes before cross-linking, the interface is a porous interface. As a general strategy for establishing theoretical models for porous fibrous materials,[29–31] we simplify the surface of cross-linked PVA/PAN membranes into two-dimensional square pores with uniform periodic distribution. Due to its seamless integration with the electrode material, the model of electrodes is designed as a complementary periodic protrusion structure. As for the traditional flat stacking structure, the electrode and electrolyte are both modeled as simple two-dimensional flat planes. The cross-sectional diagrams of the interfaces of the two structures are depicted in Fig. 3d. The stress distribution of the device under bending deformation shows that stress tends to concentrate at bending points in flat stacking structures, leading to a high susceptibility of electrode structures to damage and separation from the electrolyte. In contrast, for this porous all-in-one structure, stress is distributed throughout the entire porous interface, circumventing the destruction of electrode materials and interfacial structures caused by high stress. And the friction

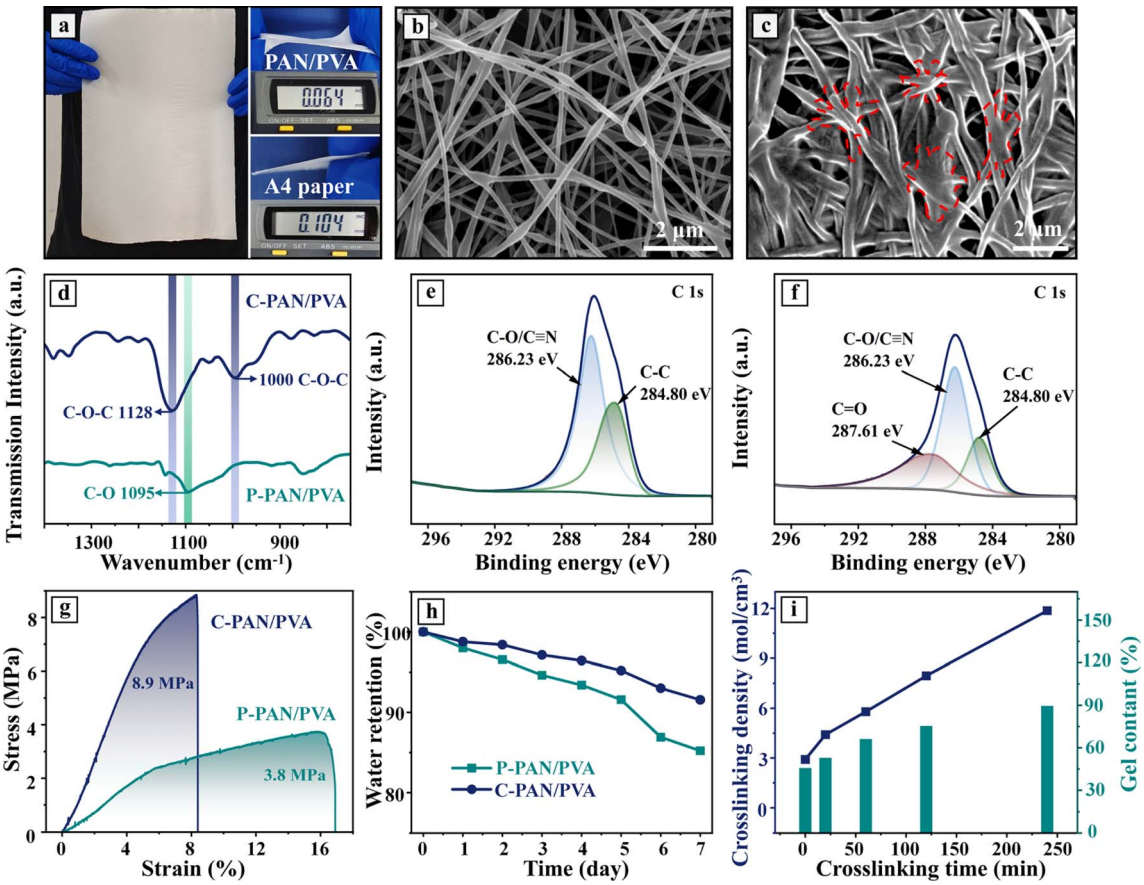

Fig. 2 Characterization of PAN/PVA membrane. (a) Photographs of the PVA/PAN membrane and the thickness measurement of the C-PVA/PAN membrane and A4 paper. (b) SEM images of P-PAN/PVA and (c) C-PAN/PVA. (d) FTIR spectra of P-PAN/PVA and C-PAN/PVA. (e) XPS C 1s spectrum of P-PAN/PVAg. (f) XPS C 1s spectrum of C-PAN/PVA. (g) The stress–strain curves of P-PAN/PVA and C-PAN/PVA. (h) The water retention rate of P-PAN/PVA and C-PAN/PVA. (i) The cross-linking density and gel content of PAN/PVA under different cross-linking times.

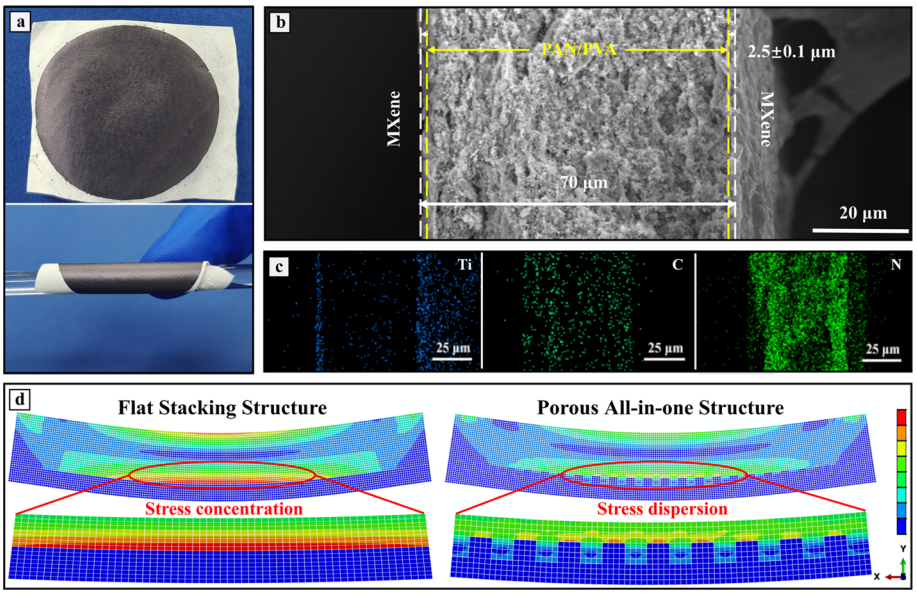

Fig. 3 Morphology characterization and electrochemical performance of MXene SSC. (a) Photographs of fabricated MXene SSC showing good flexibility. (b) SEM images and (c) corresponding element mappings of a cross-sectional view of MXene SSC. (d) Mechanical simulation of the traditional flat stacking structure and the porous all-in-one structure.

between the integrated electrode–electrolyte interface avoids their separation. Therefore, this all-in-one structure disperses stress and achieves a secure fixation of the electrode–electrolyte interface.

To assess the electrochemical performance of the MXene SSCs, Fig. 4a presents the CV curves of SSCs with different cross-linking times (0, 10, 30, 60, 120, and 240 minutes). The devices operate within a stable voltage window of 0–0.6 V, featuring a pair of prominent redox peaks likely due to the intercalation and deintercalation of H^+ between the MXene layers. The integral area of the CV curve indicates that the C-PAN/PVA electrolyte cross-linked for 1 hour exhibited the highest capacitance. Furthermore, the trend of the device-specific capacitance initially increasing and then decreasing with the extension of cross-linking time can be interpreted as the formation of C-PAN/PVA hydrogel promoting the accommodation of the electrolyte and the intimate bonding at the interface. However, an overly extended cross-linking duration leads to excessive fiber cross-linking, resulting in pore obstruction and a reduction in the active interface area. GCD curves (Fig. S1†) reveal its high gravimetric specific capacitances of 100, 90, 75.5, and 59.1 at current densities of 1, 2, 3, and 5 A g^{-1}. The impedance spectrum in Fig. 4b consists of a semicircle in the high-frequency region and a vertical line to the *X*-axis in the low-frequency region, and the equivalent series resistance of 0.646 Ω, indicating the high ion transfer efficiency of the device. The low charge transfer resistance of 8.871 Ω exhibits the fast transfer of electrons across tight interfaces, demonstrating the advantage of this integrated structure. Long-term cycling tests indicate that the MXene SSC maintains 86% of its initial capacitance after 10 000 charge–discharge cycles (Fig. 4c).

The thickness of the electrode layer of MXene SSCs can be precisely controlled by adjusting the concentration of MXene suspension used for vacuum filtration, thereby further regulating the electrochemical performance of MXene SSCs. Electrochemical tests were conducted on MXene SSCs with different electrode loadings of 0.8, 1.6, 3.2, and 4.8 mg cm^{-3}. Fig. 4d shows the CV curves of MXene SSCs with various loadings at a scan rate of 50 mV s^{-1}. The integral area of the CV curve indicates that the device with a loading of 0.8 mg cm^{-3} exhibits the highest specific capacitance. Fig. 4e and f present that the SSC with a loading of 0.8 mg cm^{-3} has a larger specific

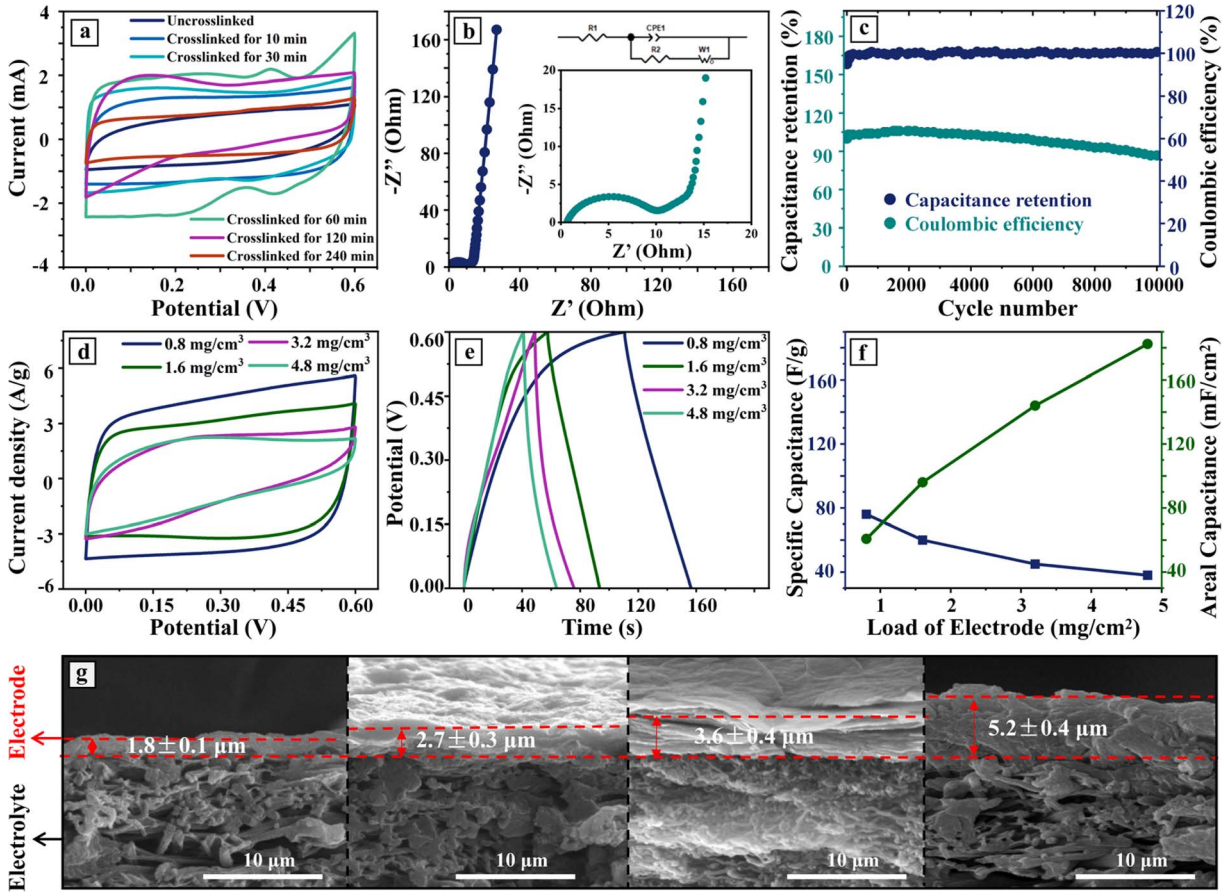

Fig. 4 The morphological characterization and electrochemical performance of MXene SSCs at different electrode loadings. (a) CV curves of the MXene SSC based on C-PAN/PVA under different cross-linking times at a scan rate of 10 mV s^{-1}. (b) EIS curves of the MXene SSC. (c) Cycle performance of the MXene SSC. (d) The CV curves of C-PAN/PVA-based MXene SSC at different electrode loadings under a scan rate of 50 mV s^{-1}. (e) The GCD curves of the device at different electrode loadings under a current density of 1 A g^{-1}. (f) The specific mass capacitance and areal capacitance performance of MXene SSC at various electrode loadings. (g) The SEM images of the cross-sections of MXene SSC electrodes prepared with loadings of 0.8, 1.6, 3.2, and 4.8 mg cm^{-3}, respectively.

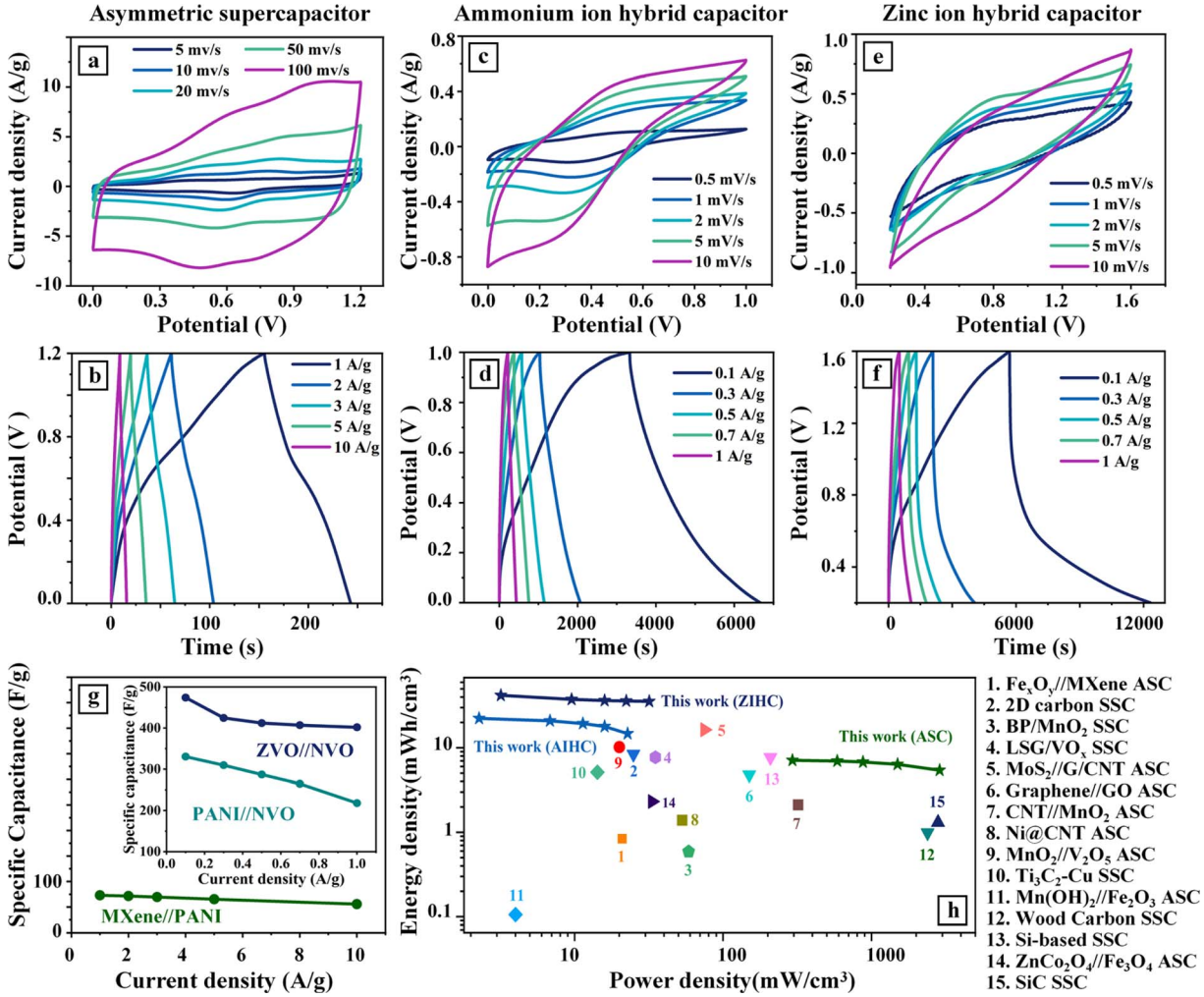

Fig. 5 Electrochemical performance of all-in-one asymmetric and hybrid electrochemical capacitors. (a) CV curves and (b) GCD curves of MXene//PANI ASC. (c) CV curves and (d) GCD curves of PANI//NVO AIHC with 1 M $(NH_4)_2SO_4$ as electrolyte. (e) CV curves and (f) GCD curves of ZVO//NVO ZIHC with 1 M $Zn(OTf)_2$ as electrolyte. (g) The specific capacitance of the ASC, AIHC, and ZIHC as a function of current densities. (h) Comparison of performance between our work with other reported sandwich-structured electrochemical capacitors.[32–46]

capacitance, while the SSC at a loading of 4.8 mg cm^{-3} exhibits the highest areal capacitance of 182 mF cm^{-2}. SEM images in Fig. 4g show the cross-section of MXene layers with loadings of 0.8, 1.6, 3.2, and 4.8 mg cm^{-3} loaded on the C-PAN/PVA membrane. The thickness of the electrodes was calculated by averaging the values from three selected points on each sample. It can be observed that the average thickness of the MXene layer gradually increases from 1.8 μm to 5.2 μm, demonstrating the precise control of the electrode loading through this strategy. Therefore, augmenting the thickness of the electrode layer can improve the total capacitance of the device. When divided by the identical electrode area, the device with increased thickness demonstrates superior areal capacitance. But the increase in electrode layer thickness reduces the gravimetric capacitance, which can be attributed to the difficulty of ions penetrating through the thick MXene layer, resulting in insufficient participation of the thick electrode in energy storage, rendering further increased electrode loading unnecessary. Simultaneously, the device displays diminished coulombic efficiency under low electrode thickness due to the poor film formation of the MXene electrodes at low loadings and the side reactions occurring at low current densities. Hence, subsequent implementations adopted a moderate loading of 1.6 mg cm^{-3}.

Since the vacuum filtration technique offers convenience in fabricating electrodes, asymmetric supercapacitors (ASCs) are fabricated, where MXene serves as the negative electrode material and PANI acts as the positive electrode material (Fig. S2a†). Fig. 5a displays the CV curves for MXene//PANI ASC at various scan rates (5–100 mV s^{-1}), demonstrating stable and ideal capacitive behavior at a high potential window of 1.2 V. In Fig. 5b, the non-linear GCD curves further reveal pseudocapacitive characteristics of the MXene//PANI ASC. The gravimetric specific capacitance for MXene//PANI ASC is 73, 71.6, 69.5, 65.4, and 55.8 F g^{-1} at current densities of 1, 2, 3, 5, and 10 A g^{-1}. Moreover, ammonium ion hybrid capacitors (AIHCs) with PANI as the negative electrode and $NH_4V_4O_{10}$ (NVO) as the positive electrode, as well as zinc ion hybrid capacitors (ZIHCs) with $Zn_3V_3O_8$ (ZVO) as the negative electrode and $NH_4V_4O_{10}$ (NVO) as

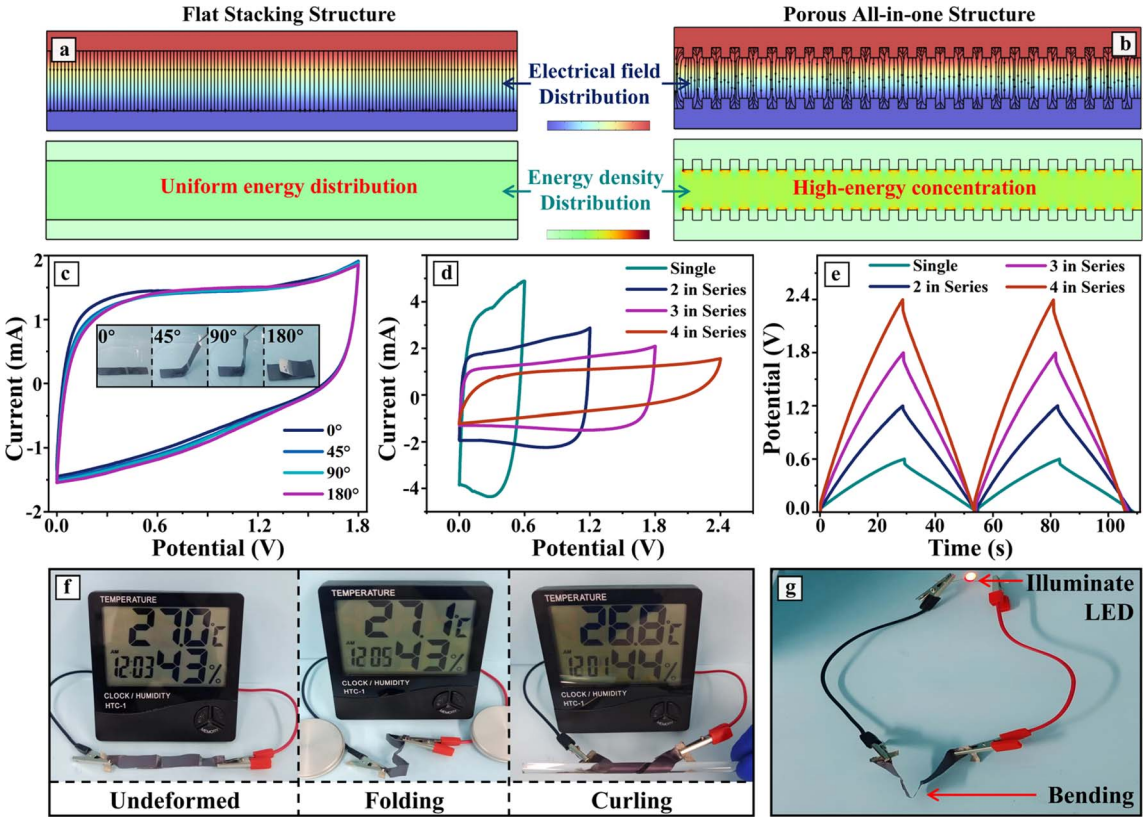

Fig. 6 Electrochemical performance of MXene SSC after series connection. (a) Electrical field and (b) energy density simulation of the traditional flat stacking structure and the porous all-in-one structure. (c) CV curves recorded at 20 mV s^{-1} under bending from 0° to 180° (inset: optical images under different bending angles). (d) CV curves of the MXene SSC assembled with multiple cell units in series at a scan rate of 50 mVs^{-1}. (e) GCD curves of the MXene SSC assembled with multiple cell units in series at a current density of 1 A g^{-1}. (f) Photographs of the series-connected SSCs operating a thermo-hygrograph in the fording and twisting states. (g) Photographs of the series-connected SSCs illuminate the light bulb.

the positive electrode, were prepared using the same strategy (Fig. S2b and c†). Fig. 5c and e illustrate the CV curves of PANI//NVO AIHC and ZVO//NVO ZIHC at different scan rates (0.5 mV s^{-1} to 10 mV s^{-1}), which GCD curves confirming excellent electrochemical reversibility are shown in Fig. 5d and f. Calculating from the GCD curves, the PANI//NVO AIHC and ZVO//NVO ZIHC exhibit high coulombic efficiency of nearly 100% and outstanding maximum specific capacitances of 330.5 F g^{-1} and 474.1 F g^{-1}, respectively. As summarized in Fig. 5g, all three all-in-one electrochemical capacitors exhibited excellent rate performances, where the PANI//NVO AIHC and ZVO//NVO ZIHC display capacitance retention of 66.0% and 84.8% as the current densities increased from 0.1 to 1 A g^{-1}, while MXene//PANI ASC shows capacitance retention of 76.4% as the current densities increased from 1 to 10 A g^{-1}. Then, the energy and power performances of the devices are further calculated in Fig. 5h. Benefiting from the all-in-one design based on the ultra-thin fibrous membrane, the device possesses a compact overall volume. Consequently, when calculated based on the total volume of the device, the ZVO//NVO ZIHC exhibits the highest volumetric energy density of 41.8 mW h cm^{-3} (at a volumetric power density of 3.2 mW cm^{-3}) and the PANI//MXene ASC shows the highest volumetric power density of 2873 mW cm^{-3} (at a volumetric energy density of 5.42 mW h cm^{-3}), which is outstanding compared to other reported sandwich-structured electrochemical capacitors (Table S2†).

Furthermore, finite element simulations were carried out by using COMSOL software to prove the effectiveness of this all-in-one structure on device performance. As shown in Fig. 6a, in contrast to traditional flat interfaces, this integrated porous interface possesses a larger electrode–electrolyte interface area, resulting in more active sites. Therefore, the all-in-one device exhibits a greater specific capacitance and energy density (Fig. 6b) than traditional electrochemical capacitors. Moreover, benefiting from the flexibility endowed by this structure, the device maintains stable performance and shows negligible capacitance decay under bending from 0° to 180° (Fig. 6c). For practical application, an integrated series-connected SSC is fabricated by interleaving and compressing C-PAN/PVA hydrogel membranes loaded with MXene on a single side, where MXene acts as both the electrodes and the conductive connection between the SSCs (Fig. S4†).[47] Fig. 6d depicts the CV curves of the overall configuration after connecting two or four devices in series. Evidently, by serially connecting devices, the voltage could reach 1.2 V or 2.4 V, fulfilling the power requirements. Fig. 6e presents GCD curves of the connected devices, indicating excellent charge–discharge reversibility even at high voltages. After connecting MXene SSCs in series, the device enables the

successful powering of a temperature-humidity sensor and an LED under various deformation (Fig. 6f and g).

3. Conclusion

We have utilized an *in situ* cross-linking method to construct all-in-one flexible electrochemical capacitors featuring a close interface between hydrogel electrolytes and diverse electrode materials. Through this strategy, MXene SSCs were prepared with an ultra-thin thickness of 70 μm, controllable electrode thickness, and rapid interfacial ion transport. Then, finite element simulations have demonstrated the inherent advantages of this all-in-one structure in terms of high energy density and flexibility. Additionally, different asymmetric and hybrid electrochemical capacitors were prepared based on this strategy, exhibiting the highest volumetric energy density of 41.8 mW h cm^{-3} (ZVO//NVO ZIHC) and the highest volumetric power density of 2873 mW cm^{-3} (PANI//MXene ASC). Moreover, serial connections enabled the integrated electrochemical capacitors to power electrical devices under complex deformations such as folding and curling. In conclusion, this universal approach for constructing different types of ultra-thin all-in-one flexible electrochemical capacitors holds promise for widespread application in future wearable electronic devices.

4. Experimental section

4.1 Materials

Dimethyl sulfoxide (DMSO), ammonium sulfate, ammonium persulfate, ammonium metavanadate (NH_4VO_3), oxalic acid dihydrate, and lithium fluoride (LiF) were purchased from Shanghai Aladdin Bio-Chem Technology Co. Ltd. Polyvinyl alcohol (PVA, $M_w \sim 205\,000$), polyacrylonitrile (PAN, $M_w \sim 150\,000$), aniline, and $Zn(CH_3COO)_2$ were purchased from Shanghai Macleans Biochemical Technology Co., Ltd. Sulfuric acid (H_2SO_4) and hydrochloric acid (HCl) were used without further purification, deionized water was used for all experiments.

4.2 Preparation of PAN/PVA

A spinning solution was prepared by dissolving 1.28 g of PAN and 0.55 g of PVA in 15 mL of DMSO at 50 °C for 24 h. Electrospinning was carried out using a plastic syringe, with electrospinning parameters that included an electrospinning voltage of 20.5 kV, a spinning distance of 15 cm, and a feeding rate of 0.15 mm min^{-1}. The nanofibers were collected on a drum covered with silicon release paper.

4.3 Preparation of electrode materials

$Ti_3C_2T_x$ MXene electrode material was achieved through etching using LiF and HCl, followed by thorough cleaning and exfoliation processes, as previously reported.[48,49]

PANI was synthesized using a chemical oxidation method.[50] 4.66 g aniline was first dissolved in 50 mL of 1 mol L^{-1} HCl. Subsequently, 14.26 g of ammonium persulfate was dispersed in 26 mL of deionized water and stirred continuously in an ice bath until the temperature reached approximately 0 °C. The pre-cooled ammonium persulfate solution was then slowly added dropwise to the aforementioned monomer solution to initiate polymerization. After maintaining the reaction in the ice bath for 1 hour, the reaction product was washed and filtered using a centrifuge, followed by freeze-drying at −50 to −80 °C for 24 hours to obtain PANI powder.

NVO was synthesized using a hydrothermal method.[51] Initially, 0.546 g NH_4VO_3 and 0.589 g oxalic acid dihydrate were dissolved in 70 mL deionized water and stirred at room temperature for 1 h. Subsequently, the suspension was transferred to a Teflon-coated stainless steel container and subjected to a 2 hours hydrothermal treatment at 180 °C. Finally, the NVO product was obtained through a series of filtration and washing steps from the reaction mixture.

ZVO was synthesized by first dissolving 2.2 g $Zn(CH_3COO)_2$ and 1.17 g NH_4VO_3 in 60 mL deionized water. After stirring at 90 °C for 6 h, the solution was dried at 70 °C. ZVO powder was obtained by grinding and annealing at 750 °C for 9 hours.[52]

4.4 Fabrication of all-in-one electrochemical capacitors

MXene SSCs were prepared by vacuum filtering a measured concentration of the MXene suspension onto both sides of the PAN/PVA membrane. By diluting the MXene dispersion, the actual loading of MXene during the filtration process can be precisely adjusted, thereby controlling the thickness of the electrodes. Subsequently, they were placed in a vacuum container containing hydrochloric acid and an aqueous solution of GA, where the PVA was crosslinked with GA under acidic conditions through a vacuum process. Finally, the rapid fabrication of all-in-one capacitor devices was achieved through the immersion of the H_2SO_4 electrolyte. Asymmetric and hybrid electrochemical capacitors were fabricated following a similar method, with each side of the PAN/PVA membrane first filtering the suspension of different electrode materials with concentration that can be configured as needed, followed by an additional filtration of MXene as a conductive and reinforcing layer.

4.5 Electrochemical testing

For the electrochemical evaluation of all-in-one electrochemical capacitors, two-electrode testing was conducted by cutting the single devices into circles with a diameter of 12 mm and testing them using a Swagelok cell. The mass load ratio of the positive to negative electrode was calculated using eqn (1):

$$\frac{m_+}{m_-} = \frac{E_- \times C_-}{E_+ \times C_-} \quad (1)$$

where m_+ and m_- (mg) represent the mass loading of active materials for positive electrodes and negative electrodes, respectively. C_+ and C_- (F g^{-1}) are the gravimetric specific capacitances of active materials of positive electrodes and negative electrodes, respectively. E_+ and E_- (V) represent the working voltage range of active materials of positive electrodes and negative electrodes, respectively.

Cyclic voltammetry and galvanostatic charge–discharge testing were conducted using a Biologic workstation (VSP). Long-term cycling tests were performed using a Neware battery

testing system. The gravimetric specific capacitances were calculated using eqn (2):

$$C_m = \frac{I \times t}{\Delta V \times m} \quad (2)$$

where I is the discharge current (mA), t (s) represents the discharge time, and ΔV (V) stands for the voltage window. For the three-electrode system, m (mg) represents the mass load of active materials for positive electrodes or negative electrodes. For the electrochemical capacitors, m (mg) is the mass load of active materials in the entire supercapacitor. The gravimetric specific capacitances C_m (F g^{-1}) are calculated from galvanostatic charge–discharge tests. The volumetric energy density E_v (mW h cm^{-3}) of the assembled electrochemical capacitor was evaluated using eqn (3):

$$E_V = \frac{C_V \Delta V^2}{2 \times 3.6} \quad (3)$$

where C_v (F cm^{-3}) is the volumetric specific capacitances calculated from the volume and capacitance of the capacitor, ΔV (V) stands for the voltage window.

4.6 Swelling test

The PAN/PVA samples, treated with different cross-linking times, were cut into 10 mm × 10 mm squares. The initial mass of each sample was measured as m_0. After swelling in deionized water for one week, the mass was recorded as m_1. Finally, the samples were placed in a 60 °C oven for 24 hours and weighed again with the mass recorded as m_2. After measuring the original density of the polymer (ρ_m), and calculating the average molecular weight between cross-linking points (m_c) by the F–R equation,[53] the cross-linking density (ρ) and the gel content (W) can be calculated using eqn (4) and (5):

$$\rho = \frac{\rho_m}{m_c} \quad (4)$$

$$W = \frac{0.3 \times m_0 - (m_0 - m_2)}{0.3 \times m_0} \quad (5)$$

4.7 Characterization

SEM images were obtained using a Sirion 20 microscope with an accelerating voltage of 200 kV. XRD patterns were recorded with a DX-2700BH (Haoyuan) diffractometer. Fourier-transform infrared spectra were collected with a Thermo Scientific Nicolet iS20 instrument. XPS measurements were conducted on a K-Alpha (Thermo Fisher Scientific) spectrometer using Al Kα radiation. The tensile mechanical properties were characterized by cutting the samples into dumbbell shapes and testing them using the MTS Model E43 universal testing machine. The tensile rate was set at 0.1 mm min^{-1}.

4.8 Finite element simulation

The finite element modeling in this work was performed using ABAQUS and COMSOL software, in order to systematically reveal the internal stress during the bending process and electrochemical performance under the external electric field. The cross-sections of the two models, the flat stacking structure and the porous all-in-one structure are modeled, with their interfaces represented as flat and zigzag interfaces for differentiation, and the dimension of the electrode was set to 50 μm × 2 μm while that of the electrolyte was set to be 50 μm × 6 μm, in which the zigzag structure of 1 μm × 1 μm was introduced to the porous all-in-one structure (Fig. S3†).

The simulation parameters were generally taken from experimental data of the MXene SSC: the electrode's elastic constant was specified as 3.0 GPa, with its electronic conductivity set to be 10 000 S m^{-1}; the electrolyte's elastic constant was specified as 0.2 GPa, with its ionic conductivity set to be 10 S m^{-1}; the electrochemical window was set to be 0 V to 0.6 V.

Data availability

Data supporting this article have been included as part of the ESI† and the manuscript.

Conflicts of interest

There are no conflicts to declare.

Acknowledgements

This work is supported by the National Key Research and Development Program of China (No. 2023YFC3009502), National Natural Science Foundation of China (No. 52371134, U23A20574, No. 22408047), Natural Science Foundation of Jiangsu Province (BK20231432), Aeronautical Science Foundation of China (2023Z015069001), the Start-up Research Fund of Southeast University (No. RF1028623040), and the Fundamental Research Funds for the Central Universities (No. 2242023K40027).

References

1 Y. Rao and N. Lu, *Nature*, 2024, **628**, 39–40.
2 B. Zhang, J. Li, J. Zhou, L. Chow, G. Zhao, Y. Huang, Z. Ma, Q. Zhang, Y. Yang, C. Yiu, J. Li, F. Chun, X. Huang, Y. Gao, P. Wu, S. Jia, H. Li, D. Li, Y. Liu, K. Yao, R. Shi, Z. Chen, B. Khoo, W. Yang, F. Wang, Z. Zheng, Z. Wang and X. Yu, *Nature*, 2024, **628**, 84–92.
3 D. Zhong, C. Wu, Y. Jiang, Y. Yuan, M. Kim, Y. Nishio, C. Shih, W. Wang, J. Lai, X. Ji, T. Gao, Y. Wang, C. Xu, Y. Zheng, Z. Yu, H. Gong, N. Matsuhisa, C. Zhao, Y. Lei, D. Liu, S. Zhang, Y. Ochiai, S. Liu, S. Wei, J. Tok and Z. Bao, *Nature*, 2024, **627**, 313–320.
4 Y. Hu, M. Wu, F. Chi, G. Lai, P. Li, W. He, B. Lu, C. Weng, J. Lin, F. Chen, H. Cheng, F. Liu, L. Jiang and L. Qu, *Nature*, 2023, **624**, 74–79.
5 P. Simon and Y. Gogotsi, *Nat. Mater.*, 2020, **19**, 1151–1163.
6 W. Zhang, P. Feng, J. Chen, Z. Sun and B. Zhao, *Prog. Polym. Sci.*, 2019, **88**, 220–240.

7 T. Liu, S. Sutarsis, X. Zhong, W. Lin, S. Chou, N. Kirana, P. Huang, Y. Lo, J. Chang, P. Wu and S. Chen, *Energy Storage Mater.*, 2021, **38**, 489–498.
8 X. Ji, Q. Wang, M. Yu, M. Hadi, Y. Liu, L. Zhao and F. Ran, *Energy Storage Mater.*, 2021, **37**, 587–597.
9 T. Cheng, X.-L. Yang, S. Yang, L. Li, Z.-T. Liu, J. Qu, C.-F. Meng, X.-C. Li, Y.-Z. Zhang and W.-Y. Lai, *Adv. Funct. Mater.*, 2023, **33**, 2210997.
10 T. Cheng, Z.-T. Liu, J. Qu, C.-F. Meng, L.-J. He, L. Li, X.-L. Yang, Y.-J. Cao, K. Han, Y.-Z. Zhang and W.-Y. Lai, *Adv. Sci.*, 2024, **11**, 2403358.
11 T. Cheng, F. Wang, Y.-Z. Zhang, L. Li, S.-Y. Gao, X.-L. Yang, S. Wang, P.-F. Chen and W.-Y. Lai, *Chem. Eng. J.*, 2022, **450**, 138311.
12 M. M. Baig, S. A. Khan, H. Ahmad, J. Liang, G. Zhu, H. Pang and Y. Zhang, *FlexMat*, 2024, **1**, 79.
13 Y. Ren, Y. Liu, S. Wang, Q. Wang, S. Li, W. Wang and X. Dong, *Carbon Energy*, 2022, **4**, 527–538.
14 L. Chen, Z. Huang, H. Liang, W. Yao, Z. Yua and S. Yu, *Energy Environ. Sci.*, 2013, **6**, 3331–3338.
15 J. Zeng, L. Dong, W. Sha, L. Wei and X. Guo, *Chem. Eng. J.*, 2020, **383**, 123098.
16 Q. Gong, Y. Li, X. Liu, Z. Xia and Y. Yang, *Carbohydr. Polym.*, 2020, **245**, 116611.
17 H. Wan, C. Qin and A. Lu, *J. Mater. Chem. A*, 2022, **10**, 17279–17287.
18 X. Gao, Q. Hu, K. Sun, H. Peng, X. Xie, H. Hamouda and G. Ma, *J. Alloys Compd.*, 2021, **888**, 161554.
19 Q. Hu, S. Cui, K. Sun, X. Shi, M. Zhang, H. Peng and G. Ma, *J. Energy Storage*, 2022, **50**, 104231.
20 S. Cui, Y. Lv, Y. Jia, Q. Hu, W. Hou, W. Miao, X. Shi, K. Sun, H. Peng and G. Ma, *J. Energy Storage*, 2023, **68**, 107877.
21 Y. Huanga and S. Bian, *J. Mater. Chem. A*, 2021, **9**, 21347–21356.
22 P. Du, X. Hu, C. Yi, H. Liu, P. Liu, H. Zhang and X. Gong, *Adv. Funct. Mater.*, 2015, **25**, 2420–2427.
23 T. Gao, Z. Zhou, J. Yu, D. Cao, G. Wang, B. Ding and Y. Li, *ACS Appl. Mater. Interfaces*, 2018, **10**(28), 23834–23841.
24 Z. Kaberova, E. Karpushkin, M. Nevoralová, M. Vetrík, M. Šlouf and M. Dušková-Smrčková, *Polymers*, 2020, **12**(3), 578.
25 N. R. Richbourg and N. A. Peppas, *Prog. Polym. Sci.*, 2020, **105**, 101243.
26 B. Gao and M. Wang, *Polymer*, 2023, **283**, 126221.
27 K. Wang, X. Zhang, C. Li, X. Sun, Q. Meng, Y. Ma and Z. Wei, *Adv. Mater.*, 2015, **27**, 7451–7457.
28 A. VahidMohammadi, J. Rosen and Y. Gogotsi, *Science*, 2021, **372**, eabf1581.
29 C. Xiong, Y. Zhang, J. Xu, W. Dang, X. Sun, M. An, Y. Ni and J. Mao, *Nano Res.*, 2023, **16**, 9471–9479.
30 M. Wang, H. Wang, X. Zhang, D. Chen, N. Wang, M. Qin and J. Yang, *Appl. Surf. Sci.*, 2023, **636**, 157820.
31 C. Wang, Y. Li, F. Cao, Y. Zhang, X. Xia and L. Zhang, *ACS Appl. Mater. Interfaces*, 2022, **14**(8), 10457–10466.
32 A. M. Patil, S. Moon, A. A. Jadhav, J. Hong, K. Kang and S. C. Jun, *Adv. Funct. Mater.*, 2023, **33**, 2305264.
33 L. Yao, Q. Wu, P. Zhang, J. Zhang, D. Wang, Y. Li, X. Ren, H. Mi, L. Deng and Z. Zheng, *Adv. Mater.*, 2018, **30**, 1706054.
34 Q. Yin, H. Jia, G. Liu and Q. Ji, *Adv. Funct. Mater.*, 2022, **32**, 2111177.
35 A. Huang, M. F. El-Kady, X. Chang, M. Anderson, C.-W. Lin, C. L. Turner and R. B. Kaner, *Adv. Energy Mater.*, 2021, **11**, 2100768.
36 Z. Bo, X. Cheng, H. Yang, X. Guo, J. Yan, K. Cen, Z. Han and L. Dai, *Adv. Energy Mater.*, 2022, **12**, 2103394.
37 F. Liu, L. Zeng, Y. Chen, R. Zhang, R. Yang, J. Pang, L. Ding, H. Liu and W. Zhou, *Nano Energy*, 2019, **61**, 18–26.
38 Y. Wang, S. Y. Su, L. J. Cai, B. C. Qiu, N. Wang, J. Xiong, C. Yang, X. M. Tao and Y. Chai, *Adv. Energy Mater.*, 2019, **9**, 1900037.
39 Y. Jiang, C. Zhou and J. Liu, *Energy Storage Mater.*, 2018, **11**, 75–82.
40 L. Lyu, K. Seong, J. Kim, W. Zhang, X. Jin, D. Kim, Y. Jeon, J. Kang and Y. Piao, *Nano-Micro Lett.*, 2019, **11**, 88.
41 Y. Bai, C. Liu, T. Chen, W. Li, S. Zheng, Y. Pi, Y. Luo and H. Pang, *Angew. Chem., Int. Ed.*, 2021, **60**, 25318.
42 J. Li, S. Luo, B. Zhang, J. Lu, W. Liu, Q. Zeng, J. Wan, X. Han and C. Hu, *Nano Energy*, 2021, **79**, 105410.
43 F. Wang, J. Y. Cheong, J. Lee, J. Ahn, G. Duan, H. Chen, Q. Zhang, I.-D. Kim and S. Jiang, *Adv. Funct. Mater.*, 2021, **31**, 2101077.
44 R. S. Gao, J. Tang, X. L. Yu, S. Q. Lin, K. Zhang and L.-C. Qin, *Adv. Funct. Mater.*, 2020, **30**, 2002200.
45 D. Kong, Y. Wang, S. Huang, J. Hu, Y. Lim, B. Liu, S. Fan, Y. Shi and H. Yang, *Energy Storage Mater.*, 2019, **23**, 653–663.
46 W. Li, Q. Liu, Z. Fang, L. Wang, S. Chen, F. Gao, Y. Ji, W. Yang and X. S. Fang, *Adv. Energy Mater.*, 2019, **9**, 1900073.
47 Y.-Z. Zhang, Y. Wang, Q. Jiang, J. K. El-Demellawi, H. Kim and H. N. Alshareef, *Adv. Mater.*, 2020, **32**, 1908486.
48 Q. Xie, C. Yi, H. Zhang, H. Xia, G. Xu, C. Miao, L. Yang, T. Shui, W. Zhang and Z. Sun, *Adv. Energy Mater.*, 2024, **14**, 2303592.
49 H. Zhang, P. Chen, H. Xia, G. Xu, Y. Wang, T. Zhang, W. Sun, M. Turgunov, W. Zhang and Z. Sun, *Energy Environ. Sci.*, 2022, **15**, 5240–5250.
50 H. Park, T. Kim, J. Huh, M. Kang, J. Lee and H. Yoon, *ACS Nano*, 2012, **6**(9), 7624–7633.
51 Y. Lu, Z. Wang, M. Li, Z. Li, X. Hu, Q. Xu, Y. Wang, H. Liu and Y. Wang, *Adv. Funct. Mater.*, 2024, **34**, 2310966.
52 J. Wu, Q. Kuang, K. Zhang, J. Feng, C. Huang, J. Li, Q. Fan, Y. Dong and Y. Zhao, *Energy Storage Mater.*, 2021, **41**, 297–309.
53 J. Louf, N. B. Lu, M. G. O'Connell, H. J. Cho and S. S. Datta, *Sci. Adv.*, 2021, **7**, eabd2711.